Free-flight testing of proximal spheres and cubes in Mach 14 hypersonic flow

Dániel G. Kovács[⋆§†] *and Guillaume Grossir*[⋆] *and Grigorios Dimitriadis*[§⋆] *and Olivier Chazot*[⋆]

[⋆]*von Karman Institute for Fluid Dynamics*
Waterloosesteenweg 72, B-1640, Sint-Genesius-Rode, Belgium

[§] *University of Liège*
Allée de la Découverte 9, B-4000, Liège, Belgium

daniel.gabor.kovacs@vki.ac.be · guillaume.grossir@vki.ac.be · gdimitriadis@uliege.be · olivier.chazot@vki.ac.be
[†]Corresponding author

Abstract

Free-flight testing in hypersonic wind tunnels has shown good capabilities for analyzing the flight of debris objects and scenarios for their separation. The free-flight methodology implemented in the VKI Longshot facility was recently updated to facilitate the aerodynamic analysis of trajectories with six degrees of freedom. The image processing algorithms are extended in the present work to carry out separation studies where the models can present overlapping configurations. A dual-camera setup and the new routines proved suitable for tracking the motion of two spheres and cubes undergoing interactions. The experimental results confirm that when non-spherical geometries interfere, the separation behavior is case-dependent and sensitive to the objects' orientation.

1. Introduction

Free-flight testing techniques in short-duration hypersonic wind tunnels have demonstrated effectiveness in establishing accurate aerodynamic databases of typical space debris shapes presenting random entry attitudes and in testing fragment separation scenarios. In the free-flight methodology, the model is exposed to the flow without structural constrains, such as a sting support. Upon the arrival of the wind, the initial suspensions (e.g., support wires, a sabot, or a Chebyshev table) are removed, and the model performs a free flight according to the forces and moments imposed by the fluid and gravity. The analysis of the model's aerodynamic properties relies on the inspection of the flight trajectory by optical techniques[4, 11, 20] involving high-speed cameras or by measuring the accelerations directly with built-in sensors.[2, 6, 21] Optical methods can be divided into contour detection-based,[1, 4, 7, 11, 16] or marker-based stereo tracking[14, 15, 18, 20] approaches. Free-flight testing is well-suited for testing single bodies, multi-body separation scenarios, and essentially provides support-interference-free test conditions.

Re-entry estimation software packages (e.g., DAS, ORSAT, SESAM, DEBRISK, SCARAB, PAMPERO, etc.) are developed to promote the design of completely demisable spacecraft and hence mitigate the growth of space debris. These tools rely on low fidelity models to compute the atmospheric entry trajectory using aerodynamic databases of generic shapes or on simplified theories, e.g., modified Newtonian method,[13] which fail when the geometries are complex (e.g., hollow and concave surfaces), or if shock interactions take place between multiple objects. The toolkits compute the thermal loads, analyze their effects in terms of fragmentation and demiseability and predict the ground footprint. The applied engineering correlations are well-suited for single bodies, but due to the complex flow structures, fail in modeling the dispersion of fragments undergoing mutual interactions. Studies investigating the mutual interference of two spheres,[10, 12, 19] two bodies of various shapes,[8, 16] and sphere clusters,[17, 22] proved that the interactions between disintegrated spacecraft components or meteorite fragments can increase the lateral velocities of the pieces, which enhances object spreading. Given that, neglecting these interactions leads to the poor initialization of the debris trajectories, causing faulty demise and ground footprint predictions.

In order to enhance the accuracy of the predictions, improved dynamic separation models are required, and the current activities in the VKI Longshot wind tunnel are pursuing this goal. The aim of the study is to extend the capabilities of the free-flight methodology implemented in the Longshot to test a modest number of mutually interfering bodies. Further goals are to test the separation scenario of two spheres, and investigate the interaction of two cubes. The experiments are carried out using the recently developed dual optical setup,[7] using a horizontal schlieren system coupled with a backlit vertical view. The challenge imposed by such experiments resides in the fact that the bodies can

instantaneously overlap, making it it difficult to determine their position and attitude. The structure of the paper is as follows. Section 2 introduces the VKI Longshot facility and the optical tracking-based free-flight testing methodology. The test configurations of the experimental campaign are introduced in Section 3. Section 4 presents the measurements, and Section 5 summarizes and concludes the work.

2. Experimetal tools

2.1 VKI Longshot facility

The main facility at the von Karman Institute (VKI) for hypersonic free-flight testing of space debris objects is the VKI Longshot, illustrated in Fig. 1. The facility is operating based on the principle of a gun tunnel, and it is capable of reproducing the high Mach and large Reynolds numbers encountered during atmospheric re-entry flights. The wind tunnel's main components are a driver tube, a piston, a driven tube, a small reservoir, the hypersonic nozzle, and a test section. Since the test gas is continuously expanded through the nozzle while the volume of the reservoir is kept constant, the stagnation conditions progressively decay in time.[3] The Longshot can be operated with different test gases such as nitrogen, carbon dioxide or even helium, given that the simulation of Earth and Martian[5] entries are both possible. The wind tunnel is equipped with three interchangeable hypersonic nozzles: a Mach 10-20 conical nozzle (with various compatible nozzle throats), a Mach 12 contoured nozzle, and a Mach 14 contoured nozzle.
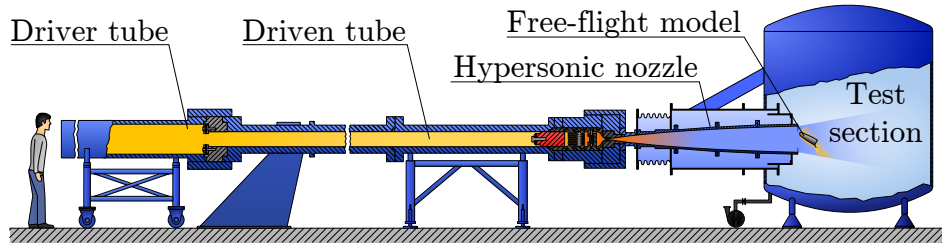

Figure 1: Schematic of the VKI Longshot facility.[4]

The present experimental campaign was carried out using the recently commissioned[9] Mach 14 contoured nozzle and nitrogen test gas. To accurately quantify the flow conditions and hence the derived quantities, such as the freestream flow speed, dynamic pressure, and aerodynamic coefficients, a freestream rebuilding technique has been developed[3] for the VKI Longshot. Freestream probes (pitot, heat-flux, and static pressure) facilitate the characterization of the flow without relying on reservoir measurements or assumptions such as adiabatic and isentropic nozzle flow expansion, yielding better accuracies on the quantities of interest. The probes are crucial when testing at non-calibrated operational points of the facility; however, they must be placed to minimize interactions with the test articles. The targeted facility conditions were calibrated previously, and provide unit Reynolds numbers decreasing from $Re_{unit} = 2.3 \cdot 10^6$ 1/m to $1.9 \cdot 10^6$ 1/m, with a core flow diameter of 280 mm for 11 ms and 200 mm for 17 ms.[9] Since the separation (spreading) of large models (with sizes of $l_{ref} = 35 - 60$ mm) initiating from a compact configuration is of interest, it is important to maintain a large unperturbed test volume and to minimize any interaction of the flow in this volume with free stream probes. Therefore, only the Pitot probe was used during the current campaign to measure the freestream, and the corresponding flow speed and temperature were recovered based on the Pitot trace, relying on repeatability from the nozzle calibration.[9]

2.2 Free-flight testing

The free-flight test setup of the VKI Longshot is illustrated in Fig. 2 with a drawing, and in Fig. 3 with images. The tracking methodology relies on a contour-based model position and attitude detection algorithm, therefore only the silhouette of the test models is of interest. The horizontal optical view is provided by the Z-type schlieren system of the wind tunnel. The illumination is supplied by a continuous Cree Xlamp XM-L LED, and a system of parabolic and flat mirrors directs the light rays through the test section and refocuses them afterwards to a Phantom v7 high-speed camera equipped with a 200 mm objective. The images were recorded at 5 kHz sampling rate at a resolution of 800×568 pixels. The schlieren system was calibrated using a scale rule, and the optical distortions were corrected based on reference images of a checkerboard plate. The second high-speed camera is positioned above the vacuum chamber, looking vertically downwards. This camera provides a backlit top view that is orthogonal to the primary, shadowgraph
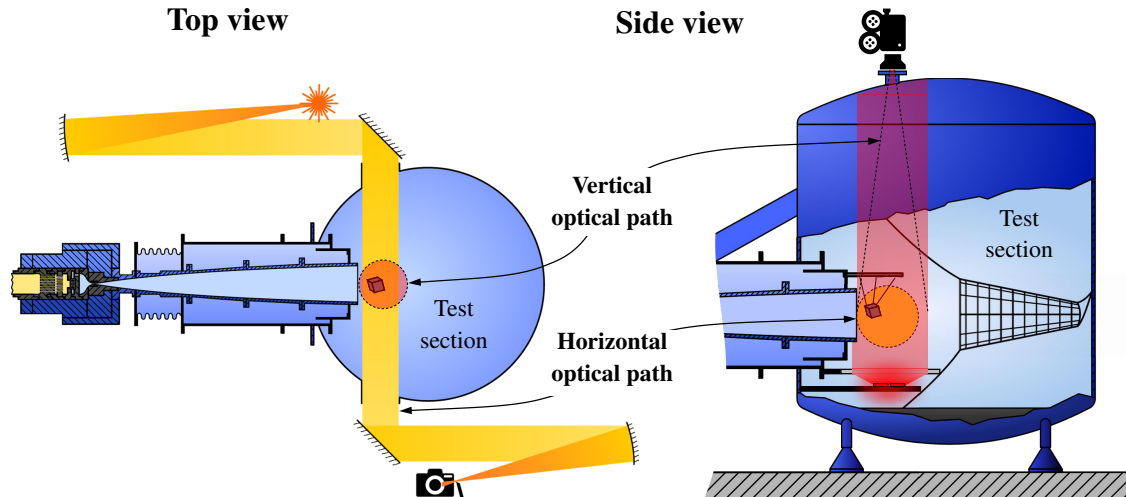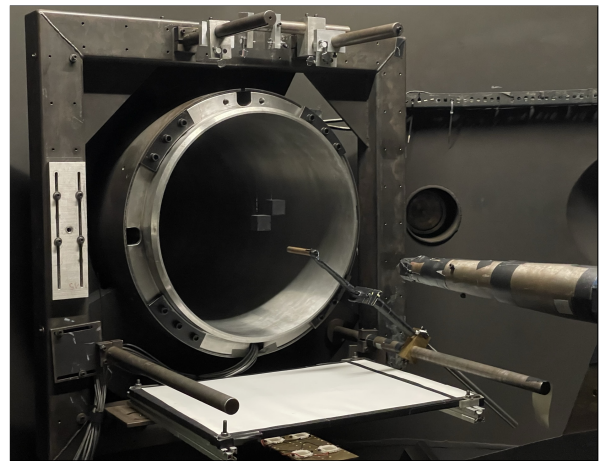
Figure 2: Top and side view schematic of the orthogonal optical paths.

(a) Top view camera positioned above the test section and side view camera facing the mirror of the schlieren system.

(b) Backlighting setup composed of LED panels and a diffusive screen.

Figure 3: Orthogonal arrangement of the cameras.[7]

view. The illumination is supplied by a matrix arrangement of high-power LED panels placed below the nozzle exit. The light sources are mounted on a brass plate functioning as a heatsink, and the illumination is homogenized with a diffusive screen placed above. The backlit images were captured using a Phantom v2012 high-speed camera with an adjustable zoom objective fixed at $200\,mm$. The experiments were recorded at $20\,kHz$ frame rate, with a resolution of 1280×800 pixels. Optical properties of the top view, such as the intrinsic parameters and the image distortions were quantified with a camera calibration.[23] Additionally, calibration images of the checkerboard plate were recorded with
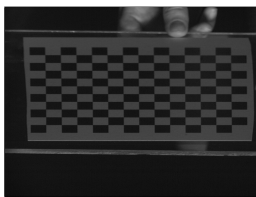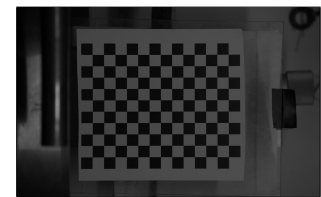

(a) Side view image of the calibration plate at arbitrary incidence.
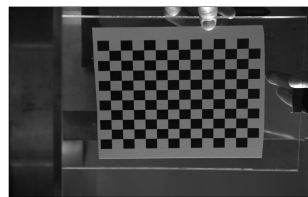
(b) Top view image of the calibration plate at arbitrary incidence
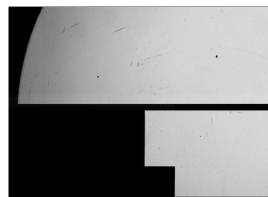
(c) Side view image of the calibration plate in the wind reference frame.

(d) Top view image of the calibration plate in the wind reference frame.

Figure 4: Calibration of the cameras and definition of wind reference frame.

FREE-FLIGHT TESTING OF PROXIMAL SPHERES AND CUBES

both cameras at the same time (Fig. 4) to correlate the position and incidence of the cameras (an example image pair is presented in Fig. 4a and 4b) and to determine the wind coordinate system (Fig. 4c and 4d).

2.3 Data processing

#### 2.3.1 Model contour detection

Processing the side and top view recordings of the experiments relies on the precise detection of the silhouettes of the test models. The contour detection procedure is illustrated in Fig. 5. First, masks are applied to the images to limit the zone of interest for the edge detection algorithm. A trajectory mask is created based on an averaged photo to surround the entire flight path (Fig. 5a) and to crop the image (Fig. 5b). Perturbing objects such as probes, shocks, or drag devices (aiding the rupture of the suspension cables) can be masked as well. This is followed by an automated masking procedure to isolate the immediate neighbourhood of the model from the background, using binarization with a strong threshold level and image noise removal. For the current study, the algorithm was extended with an additional step to merge all object boundaries to a single enclosing mask, which is presented in Figure 5c. A sub-pixel level edge
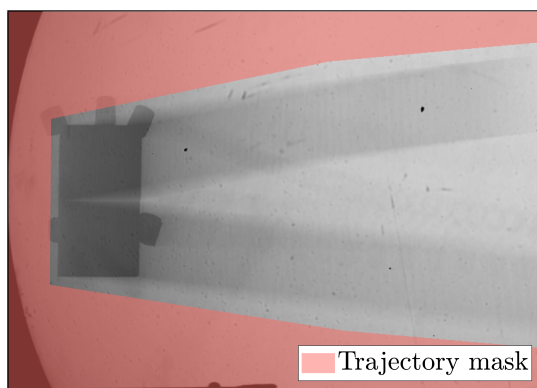
(a) Trajectory mask is created based on the average of the schlieren images.
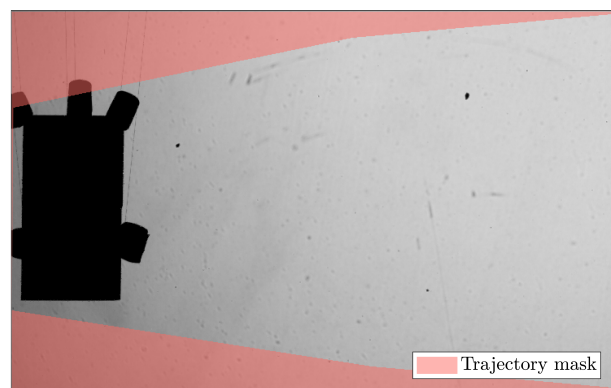
(b) Image cropped based on the trajectory mask. Further masks can be applied at this stage if required.
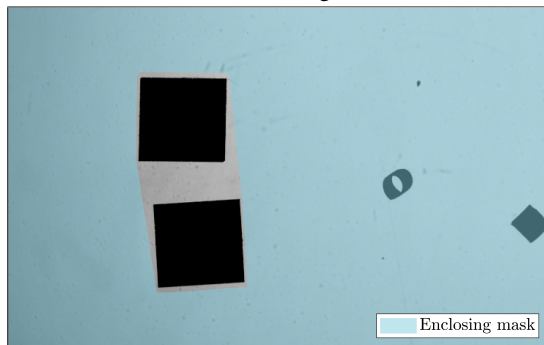
(c) Enclosing mask applied to the cropped image.

(d) Edges detected from the side view.
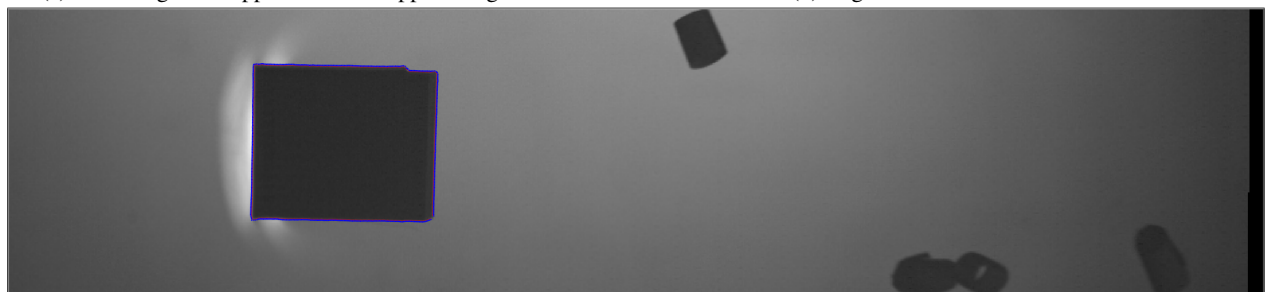
(e) Edges detected from the top view.

Figure 5: Masking and edge detection procedure applied to the side view and top view images of an experiment investigating the separation of cubes.

detection is performed on the cropped and masked images, which provides the contour points of the model shown in

Fig. 5d. The masking procedure is essentially the same for both views; however, the top view images require adaptive thresholding due to flow luminosity caused by sodium emission (bright post-shock area in Fig. 5e).

2.3.2 Identification of position and attitude

Using the CAD geometry of the test models and the calibrated camera properties, one can calculate for a given camera-respective model position (X, Y, Z) and orientation (in terms of Euler angles of ϕ – roll, θ – pitch, and ψ – yaw) the projection of the object contours into the image plane. In the shadowgraph view, the objects are mapped orthographically to the image, meaning their size in the image plane is independent of their position in the field of view, and is determined by the magnification factor. In the case of the direct view observed by the top view camera, the objects go through a perspective projection, given that their mapping onto the image plane, i.e., their size and visibility, is dependent on their camera-respective position and attitude.

Apart from the difference in the way the objects are projected, the contour matching procedure is the same for both views. Starting from an initial guess on the position and attitude of the model on the first image, the CAD geometry is projected into the image plane. The edge points of the projected contour are compared to the edge points detected on the image, by evaluating a matching error based on the distance between their coordinates. A gradient-based optimization algorithm iterates on the Euler angles and the position of the model in order to minimize the matching error. The algorithm marches through the entire set of images to estimate the flight trajectory as a function of time.

When testing with multiple objects, the position and attitude identification process can be separated for the upper and lower model if they do not overlap each other from a view angle. Since stacked model configurations were tested, this simplification could be exploited for the side view; however, in the case of the top view, the bodies presented a significant overlap throughout the experiments. Therefore, the silhouette generation algorithms were supplemented with two steps, the projection of the second model's contour, and the merging of the two contours into a single outline.

During the processing, first, the side view images are analyzed, providing the flight path in five degrees of freedom (three Euler angles, horizontal and vertical position) for both objects separately. Subsequently, the trajectory information of the bodies is supplied to the top view algorithm, which interpolates and uses them as an initial guesses for the contour matching. The top view camera has a low sensitivity in the camera-normal direction, hence the vertical positions provided by the side view processing are fixed; ten design variables, the Euler angles and the streamwise and spanwise position of both objects (X_1, Y_1, ϕ_1, θ_1, ψ_1, and X_2, Y_2, ϕ_2, θ_2, ψ_2) are optimized together.

2.3.3 Trajectory processing and computation of the aerodynamic coefficients

During the image processing, the trajectories of the models are determined in the camera's reference frames, which are transformed afterwards to the global coordinate system defined by the flow direction and the local gravitational horizontal. The velocities and accelerations of the models are derived from the free-flight trajectories in terms of global and body-fixed coordinates. Numerical differentiation of the trajectories amplifies the measurement noise, given that the signal was smoothed with a first order Savitzky-Golay filter before these computation steps. The aerodynamic forces and moments are computed in the body-fixed coordinate system according to:

$$F_{A,B} + F_{G,B} = m\dot{V}_B + \omega_B \times mV_B \,, \tag{1}$$

$$M_{A,B} = I\dot{\omega}_B + \omega_B \times I\omega_B \,, \tag{2}$$

where $F_{A,B}$ is the aerodynamic force vector, $F_{G,B}$ is the gravitational force vector, $M_{A,B}$ is the aerodynamic moment vector, m and I are the model's mass and inertia tensor, V_B and ω_B are the linear and rotational velocities, and $\dot{V}_B$ and $\dot{\omega}_B$ are the linear and rotational accelerations. The aerodynamic coefficients are computed in the body reference frame (C_x, C_y, C_z, etc.) by dividing the forces and moments with the relative freestream dynamic pressure ($q_{\infty,rel}$), the model's reference surface (S_{ref}), and reference length (l_{ref}). Using a direction cosine matrix permits the calculation of the aerodynamic properties in the wind reference frame (C_D, $C_{y,w}$, C_L, etc.).

3. Test matrix

The separation of spheres and cubes of equal dimensions was investigated in this work. Table 1 summarizes the properties of the free-flight models. The initial model configurations are illustrated with photos in Fig. 6. Two experiments were conducted with proximal spheres (Fig. 6a and 6b), and three tests focused on proximal cubes (Fig. 6c, 6d, 6e). The sphere tests and two of the cube tests were initiated from a vertical on-top configuration, while in one of one cube experiments (Figure 6e), the models were separated in both the vertical and spanwise directions. The test articles were hollow to ensure sufficient displacement during the useful test time of the wind tunnel. The models were suspended by

thin wires allowing their initial alignment. Upon the arrival of the flow, the support wires rupture due to the aerodynamic load, allowing the models fly freely. Small drag devices were placed on the suspension wires to accelerate the release process.

Table 1: Properties of the test models.

Properties	Test configurations				
	Spheres I.	Spheres II.	Cubes I.	Cubes II.	Cubes III.
Reference length	$l_{\text{ref}} = D = 40\,\text{mm}$	$l_{\text{ref}} = D = 60\,\text{mm}$	$l_{\text{ref}} = 35\,\text{mm}$		
Reference surface	$S_{\text{ref}} = D^2 \cdot \pi/4$		$S_{\text{ref}} = l_{\text{ref}}^2$		
Reference point	center of gravity				

(a) Proximal spheres test I.   (b) Proximal spheres test II.

(c) Proximal cubes test I.   (d) Proximal cubes test II.   (e) Proximal cubes test III.
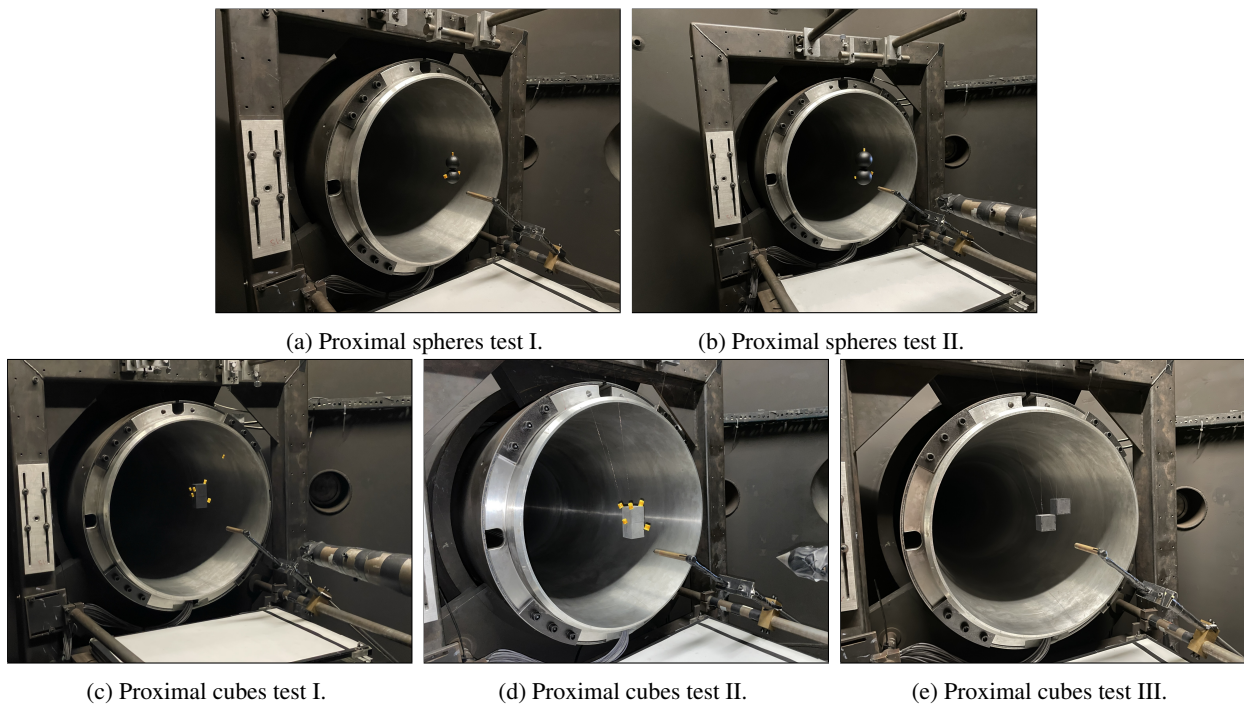
Figure 6: Model configurations of the test campaign.

4. Results and discussion

This section analyses the results of the experimental campaign in a comparative manner. The measured separation trajectories are plotted in Fig. 7, where the streamwise and vertical flight path coordinates are normalized with the models' reference length. The presented curves are truncated when the object reaches the edge of the core flow. Solid lines represent the upper models' trajectories, and dashed lines correspond to the lower ones. Observing the upper and lower model trajectories, a slight asymmetry can be seen in the case of the sphere experiments, while the cube tests present greater differences. The mean trajectories tend to curve slightly upwards. This might be due to an initial pull from the suspension wires, and the models could essentially keep that initial motion for the rest of their flight. Another reason of the asymmetry is that the influence of the shock interaction is not equal on both objects, and one contributes more to the lift of the other. Fig. 8 presents the Euler angles measured during the cube experiments. One must note that the initial yaw and roll angles of the models in Cube test I. were quite large, around $-7°$.

Figure 9 shows the variation of the models' lateral velocity as a function of time. These parameters were nondimensionalized according to Equation 3 and 4, similarly to Laurence et al.[12] and Park et al.,[16] in order to permit
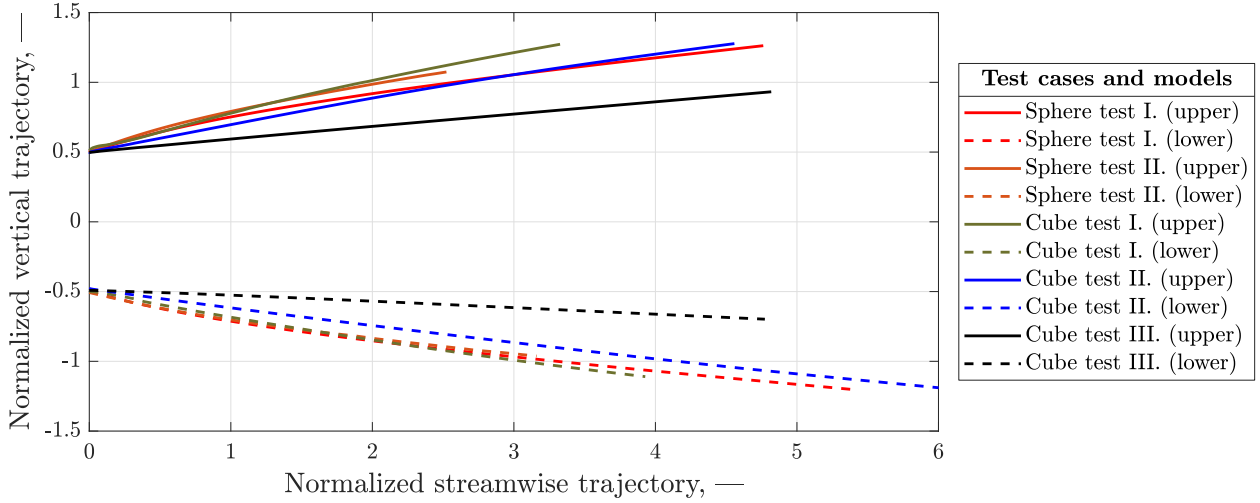
Figure 7: Separation trajectories normalized by the models' reference length.
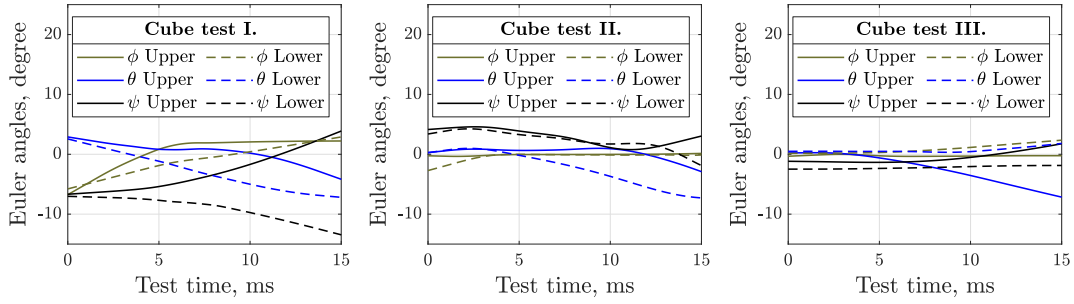

Figure 8: Euler angles of the objects during the experiments on cubes.

comparison between different test cases and campaigns. The normalized lateral velocity is computed as

$$V'_N = \sqrt{\frac{\rho_\infty}{\rho_m}} \cdot \frac{\sqrt{V_y^2 + V_z^2}}{\sqrt{(U_\infty - V_x)^2 + V_y^2 + V_z^2}} \quad , \tag{3}$$

where ρ_∞ is the freestream flow density, ρ_m is the model density, V_x, V_y and V_z are respectively the model's streamwise, vertical, and spanwise velocity, and U_∞ is the freestream flow speed. The nondimensional time is calculated from

$$t' = \sqrt{\frac{\rho_\infty}{\rho_m}} \cdot t \cdot \frac{U_\infty}{r_1} \quad , \tag{4}$$

where t is the test time, and $r_1 = l_{\text{ref}}/2$. Thin dotted and dashed curves indicate the upper and lower model's lateral velocities, and solid lines represent their average. As comparison data, the maximum lateral velocities measured by Laurence et al.[12] in Mach 4 flow and Park et al.[16] in Mach 5.7 flow are indicated with horizontal lines.

Observing Fig. 9, one can note that a terminal velocity seems to be reached only in the case of Sphere test II. and Cube test II., while the model velocities were still converging to a plateau in the case of Sphere test I. As expected, the curves for Sphere tests I. and II. look qualitatively similar. The final lateral velocities of the sphere tests are approximately in agreement with the experimental results of Laurence et al.[12] and the rough sphere measurement of Park et al.;[16] however, they are slightly higher. These small differences and the slight asymmetry of the trajectories can be attributed to the imperfections of the experimental setup, such as the upper models' release in the case of the sphere test.

The lateral velocities of the cube tests are more diverse. The models of Cube test I. presented similar final velocities ($V_{z,final} \approx 0.43$) to the ones observed by Park et al.[16] ($V_{z,max} \approx 0.415$); however, the current cuboids were still slightly accelerating. During Cube test II., the bodies reached lower terminal velocities, between ($V_{z,max} \approx 0.34 - 0.39$). This difference shows a strong dependency on the initial conditions and on the small test-to-test discrepancies in the
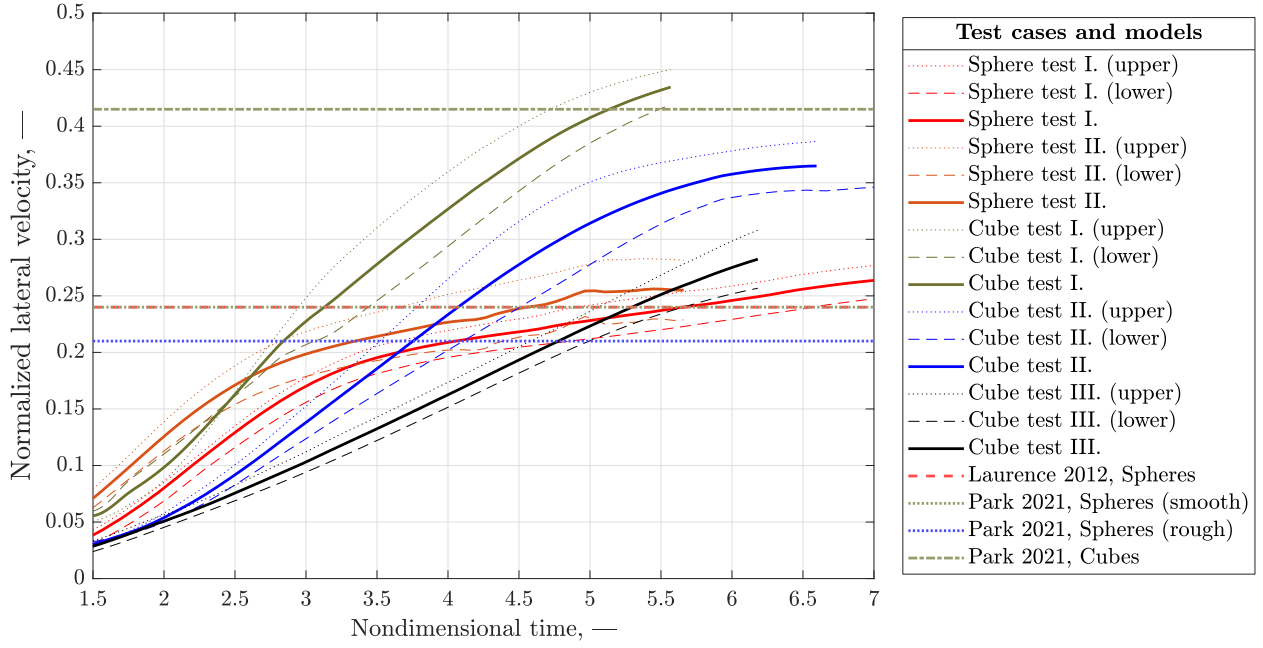
Figure 9: Lateral velocities of the separating models.

alignments. The separation velocities of the on-top cube configurations are significantly higher than the ones of the sphere experiments; moreover, greater differences are present between the motions of the upper and lower models, which is due to their unequal Euler angles. Concerning Cube test III., spacing the objects in the spanwise direction, resulted in moderate separation velocities compared to the stacked initial configurations. The reason for this behavior must be linked to the shape of their detached shock waves, so that the bodies leave each other's zone of influence over a shorter lateral distance. These results confirm the fact that when moving away from spherical geometries, the separation behavior becomes case-dependent.

The flow-normal aerodynamic forces experienced by the models are compared in Fig. 10, where the sum of the lift and wind frame side force coefficients are plotted as a function of the distance between the models. The aerodynamic coefficients were summed according to:

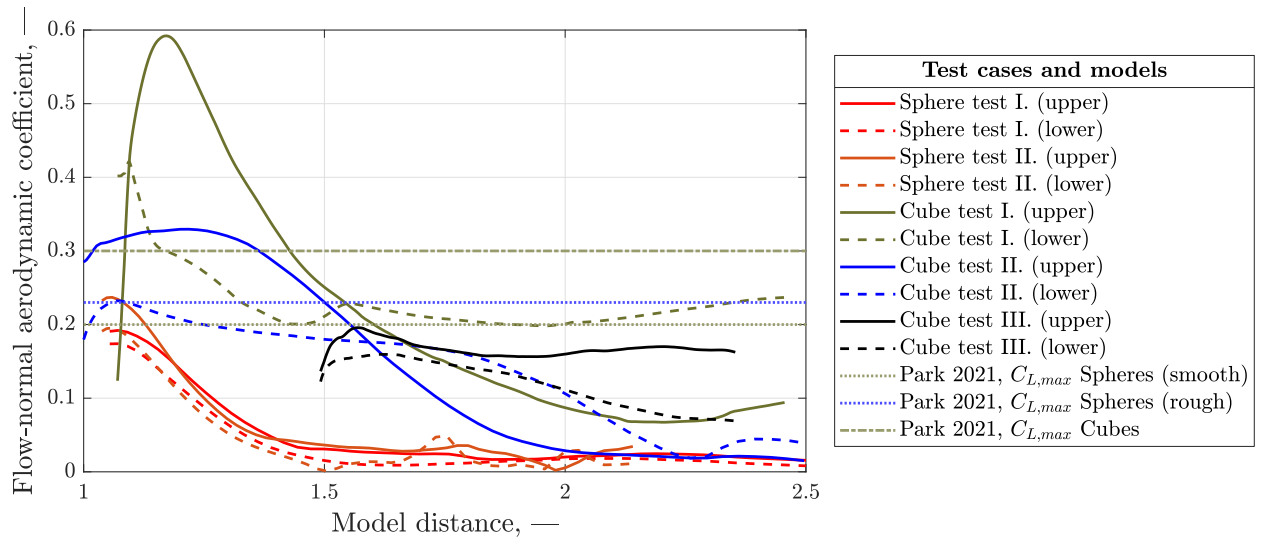$$C_N = \sqrt{C_{y,w}^2 + C_L^2} \quad , \tag{5}$$

Figure 10: Flow-normal aerodynamic coefficients as a function of the distance between the models.

and the model distances were normalized by bodies' reference length. The curves are plotted for the useful time window only, i.e., from the establishment of the flow to the time the objects leave the core flow region. The flow-normal coefficients of the sphere tests show a fair agreement, and the maxima of the curves are in close correspondence with the maximum lift coefficients found by Park et al.[16] On the other hand, the aerodynamic coefficients of the cubes are more diverse and show only initially decaying trends. The large bow shocks of the cubes exert an influence on the neighbor object for much larger lateral distances compared to the spheres. The discrepancy in the results can be attributed to the fact that the unequal Euler angles observed during the separation process would yield different aerodynamic properties even in freestream flow conditions (without interaction). This observation does not allow reaching any clear conclusions, but confirms a high degree of case-dependency.

5. Conclusions

The present work focused on the extension of the free-flight methodology implemented in the VKI Longshot wind tunnel to allow testing the separation of a modest number of objects. The updated image processing algorithms were used to track the motion of two overlapping spheres and cubes, and proved suitable for analyzing their flight. The data processing routines permit separation testing with even more objects at the expense of computational time. The application of drag devices sped up the model release process; however, the suspension system requires fine-tuning to improve the initial alignments when testing with multiple models. In order to investigate further downstream stages of multi-body separations, smaller models will be used in the future. The separation test of equal diameter spheres showed similar flow-normal velocities and aerodynamic coefficients to previous data in the literature. The experimental results confirm that when non-spherical geometries interfere, the separation behavior is case-dependent and sensitive to the objects' initial orientation.

6. Acknowledgments

References

[1] Ryan S. de Silva, Thomas J. Whalen, and Stuart J. Laurence. Free-flight optical tracking using artificial image generation. In *AIAA AVIATION 2023 Forum*, 2023.

[2] Simona Dobre, Claude Berner, Marie Albisser, F Saada, Etienne Clopeau, Luca Ferracina, and Lionel Marraffa. Marcopolo-R Erc Dynamic Stability Characterization. Open Range Free Flight Tests. *Proceedings of the 8th European Symposium on Aerothermodynamics for Space Vehicles*, 2015.

[3] Guillaume Grossir and Bruno Dias. Flow characterization of the vki longshot wind tunnel. In *Flow Characterization and Modeling of Hypersonic Wind Tunnels (STO-AVT 325)*, pages 1–32, Sint-Genesius-Rode, Belgium, November 2018. von Karman Institute for Fluid Dynamics, STO/NATO.

[4] Guillaume Grossir, Daniela Puorto, Zdeněk Ilich, Sébastien Paris, Olivier Chazot, Sébastien Rumeau, Martin Spel, and Julien Annaloro. Aerodynamic Characterization of Space Debris in the VKI Longshot Hypersonic Tunnel Using a Free-flight Measurement Technique. *Experiments in Fluids*, 61(7):163–170, 2020.

[5] Zdeněk Ilich, Guillaume Grossir, Sébastien Paris, and Olivier Chazot. Review of the VKI longshot hypersonic tunnel operation for martian entries. In *AIAA Scitech 2019 Forum*, pages 1–20, San Diego, California, USA, January 2019.

[6] Chris Kennell, Andrew Neely, Murat Tahtali, David Buttsworth, and Rishabh Choudhury. Free flight testing in hypersonic flows: HEXAFLY-INT EFTV. *54th AIAA Aerospace Sciences Meeting*, 0(January):1–13, 2016.

[7] Dániel G. Kovács, Guillaume Grossir, Grigorios Dimitriadis, and Olivier Chazot. Six degrees of freedom free-flight measurement in the vki longshot wind tunnel. In *AIAA AVIATION 2023 Forum*, pages 1–16, 2023.

[8] Dániel G. Kovács, Guillaume Grossir, Grigorios Dimitriadis, and Olivier Chazot. Space debris interaction across a two-dimensional oblique shock wave. *Manuscript in review*, 2023.

[9] Dániel G. Kovács, Zdeněk Ilich, Guillaume Grossir, and Olivier Chazot. Experimental Characterization of the VKI Longshot Mach 14 Contoured Nozzle. In *AIAA SciTech 2022 Forum*, pages 1–22. American Institute of Aeronautics and Astronautics, 2022.

[10] Stuart J. Laurence and Ralf Deiterding. Shock-wave surfing. *Journal of Fluid Mechanics*, 676:396–431, 2011.

[11] Stuart J. Laurence and Sebastian Karl. An improved visualization-based force-measurement technique for short-duration hypersonic facilities. *Experiments in Fluids*, 48:949–965, 2010.

[12] Stuart J. Laurence, Nick J. Parziale, and Ralf Deiterding. Dynamical separation of spherical bodies in supersonic flow. *Journal of Fluid Mechanics*, 713, 2012.

[13] Lester Lees. Hypersonic flow. In *5th International Aeronautical Conference*, volume 40, pages 241–276, Los Angeles, USA, 1955. AIAA.

[14] David Leiser, Stefan Löhle, Fabian Zander, David R. Buttsworth, Rishabh Choudhury, and Stefanos Fasoulas. Analysis of Reentry and Break-Up Forces from Impulse Facility Experiments and Numerical Rebuilding. *Journal of Spacecraft and Rockets*, pages 1–13, 2022.

[15] Andrew Lock, Flynn Hack, Gerard Armstrong, Ingo H Jahn, Fabian Zander, and David Buttsworth. Hypersonic aerodynamics from mach 7 free-flight tests: Initial experiments and simulations with rotating and non-rotating cubes. In *AIAA AVIATION 2023 Forum*, 2023.

[16] Seong-Hyeon Park, Junemo Kim, Ilsung Choi, and Gisu Park. Experimental study of separation behavior of two bodies in hypersonic flow. *Acta Astronautica*, 181:414–426, 2021.

[17] Seong-Hyeon Park and Gisu Park. Separation process of multi-spheres in hypersonic flow. *Advances in Space Research*, 65(1):392–406, 2020.

[18] Arianit Preci, Ali Gülhan, Etienne Clopeau, Philippe Tran, Luca Ferracina, and Lionel Marraffa. Dynamic characteristics of MarcoPolo-R Entry Capsule in low subsonic flow. *CEAS Space Journal*, 8(1):23–33, 2016.

[19] Paul J. Register, Michael J. Aftosmis, Eric C. Stern, Joseph M. Brock, Patrick M. Seltner, Sebastien Willems, Ali Gülhan, and Donovan L. Mathias. Interactions between asteroid fragments during atmospheric entry. *Icarus*, 337, 2020.

[20] Patrick M. Seltner, Sebastien Willems, and Ali Gülhan. Aerodynamic coefficients of free-flying cubes in hypersonic flowfields. *Journal of Spacecraft and Rockets*, 56(6):1725–1734, nov 2019.

[21] Hideyuki Tanno, Tomoyuki Komuro, Kazuo Sato, Katsuhiro Itoh, Masahiro Takahashi, Kazuhisa Fujita, Stuart Laurence, and Klaus Hannemann. Free-flight force measurement technique in shock tunnel. In *50th AIAA Aerospace Sciences Meeting including the New Horizons Forum and Aerospace Exposition*, page 1241, 2012.

[22] Thomas J. Whalen and Stuart J. Laurence. Experiments on the separation of sphere clusters in hypersonic flow. *Experiments in Fluids*, 62(4), 2021.

[23] Zhengyou Zhang. A flexible new technique for camera calibration. *IEEE Transactions on Pattern Analysis and Machine Intelligence*, 22(11):1330–1334, 2000.